

# Enhancing cryogenic mechanical properties of a cost-effective FeCrNi dual-phase multi-principal element alloy by fully constrained heterostructure and deformation twinning

Jinrong Wang<sup>a</sup>, Anguo Wang<sup>a,\*</sup>, Lu Zhang<sup>a,\*\*</sup>, Junyang Wang<sup>a</sup>, Li Zhang<sup>a</sup>, Rui Zhang<sup>b</sup>, Minghui Cai<sup>c</sup>, Jianxin Yu<sup>d</sup>, Baolin Wu<sup>a</sup>

<sup>a</sup> School of Materials Science and Engineering, Shenyang Aerospace University, Shenyang, 110136, Liaoning, China

<sup>b</sup> Shi-changxu Innovation Center for Advanced Materials, Institute of Metal Research, Chinese Academy of Sciences, Shenyang, 110016, Liaoning, China

<sup>c</sup> School of Materials Science and Engineering, Northeastern University, Shenyang, 110819, China

<sup>d</sup> Center of Analysis and Measurement, Harbin Institute of Technology, Harbin, Heilongjiang, 150001, China



## ARTICLE INFO

### Keywords:

Multi-principal element alloy  
Cryogenic mechanical properties  
Heterostructure  
Twinning

## ABSTRACT

This paper reports a cost-effective Fe<sub>40</sub>Cr<sub>40</sub>Ni<sub>20</sub> (at%) dual-phase multi-principal element alloy with excellent cryogenic mechanical properties. The high strength primarily originated from an ideal fully constrained heterostructure, which enhanced back stress strengthening and dislocation strengthening. Twinning enhanced the deformability and the strength of the alloy simultaneously.

## 1. Introduction

Cryogenic metal structural materials have a wide range of applications, including deep space exploration, polar scientific expeditions, cryogenic storage, and transportation. For example, the service temperature of the liquid nitrogen tank of a spacecraft rocket reaches  $-196^{\circ}\text{C}$  [1]. The storage tanks on liquefied natural gas (LNG) carriers need to work stably around  $-163^{\circ}\text{C}$  [2]. Cryogenic metal structural materials are required to have excellent mechanical properties such as high specific strength, toughness, and ductility [3–5]. As service conditions become increasingly harsh, developing new cryogenic alloys is one of the important pathways to meet the stringent requirements.

In recent years, multi-principal element alloys (MPEAs) have broken through the traditional alloy design concept based on a single element as the matrix. MPEAs exhibit excellent cryogenic mechanical properties, demonstrating the enormous potential to become a new type of cryogenic structural material [6]. Initially, researchers mainly focused on some classic single-phase face-centered cubic (FCC) MPEAs, such as the CoCrFeMnNi, CoCrFeNi, and CoCrNi series alloys. These alloys could achieve fine grains after thermomechanical treatment, exhibiting similar mechanical behavior at cryogenic temperatures, including excellent ductility and strong strain hardening ability [7–10]. At 77 K,

the CoCrNi MPEA (average grain size  $\sim 16 \mu\text{m}$ ) exhibited a yield strength of 560 MPa and a tensile strength of 1230 MPa and maintained a ductility of 45 % [7]. Similarly, the yield strength and the ultimate tensile strength of CoCrFeMnNi MPEA (average grain size  $\sim 4.4 \mu\text{m}$ ) were 566 MPa and around 1100 MPa at 77 K, respectively. It is noteworthy that the alloy maintained a high ductility close to 90 % [8]. The formation of high-density deformation twins during deformation was the main reason for the high ductility and exceptional strain hardening ability. Nonetheless, single-phase FCC MPEAs have significant drawbacks, such as low yield strength in fully recrystallized microstructure, making it difficult to meet the strength requirements for cryogenic structural materials. Researchers have recently achieved good strengthening by introducing different types of heterostructures. H. S. Kim et al. [11] successfully produced a fine-grained FCC + BCC dual-phase heterostructure in the Al<sub>0.5</sub>CoCrFeMnNi alloy through the “cold rolling + annealing” process. The volume fraction of the BCC phase was approximately 10.7 %. The grain sizes of FCC and BCC phases were 4.6 and 1.1  $\mu\text{m}$ , respectively. Compared to the aforementioned CoCrFeMnNi MPEA with a grain size of 4.4  $\mu\text{m}$ , the yield strength of the Al<sub>0.5</sub>CoCrFeMnNi alloy increased to 796 MPa at 77 K, and the ultimate tensile strength rose to 1329 MPa, but the ductility reduced to 30.5 %. The increase in strength was primarily attributed to back stress

\* Corresponding author.

\*\* Corresponding author.

E-mail addresses: [13604188303@163.com](mailto:13604188303@163.com) (A. Wang), [zhanglu5853@163.com](mailto:zhanglu5853@163.com) (L. Zhang).

strengthening due to the large strength difference between the FCC and BCC phases. Fu et al. [12] constructed a heterogeneous matrix with hierarchical B2+L1<sub>2</sub>+ $\sigma$  precipitates in an FCC Al<sub>7.5</sub>Co<sub>20.5</sub>Fe<sub>24</sub>Ni<sub>24</sub>Cr<sub>24</sub> MPEA. The alloy exhibited a high yield strength of 1109 MPa, tensile strength of 1609 MPa and elongation of 43.2 % at 77K. The excellent strength-ductility matching was attributed to the long-range back stress near soft/hard domain boundaries. It can be seen that, besides refining grain size, constructing heterostructure is also an effective method to strengthen MPEAs.

The excellent cryogenic mechanical properties make the above-mentioned MPEAs show the potential to become cryogenic structural materials. However, considering practical engineering applications, MPEAs still face two urgent issues. (1) High cost. The high Co content increases the cost. (2) High density. The density of Co and Ni is relatively high ( $\rho_{\text{Co}} = \rho_{\text{Ni}} = 8.9 \text{ g/cm}^3$ ). The high content of Co and Ni in these MPEAs leads to high alloy density, resulting in low specific strength. Consequently, reducing cost and density is an important step to accelerate the advancement of the applications of MPEAs as cryogenic structural materials. This study reports a Co-free dual-phase Fe<sub>40</sub>Cr<sub>40</sub>Ni<sub>20</sub> (at%) MPEA. The high Fe content was mainly for cost reduction. Increasing the Cr content to 40 % aimed at reducing the alloy density ( $\rho_{\text{Cr}} = 7.19 \text{ g/cm}^3$ ). The alloy exhibited a fully constrained heterostructure where the hard BCC phase enveloped the soft FCC phase in a solid solution state. High-density deformation twinning occurred in both phases during deformation. The alloy exhibited excellent cryogenic mechanical properties even in the solid solution state. The alloy saved costs from both raw materials and processing aspects. The findings of this study can provide beneficial references for the development of cryogenic MPEAs with low cost and excellent mechanical properties.

## 2. Experimental

Fe<sub>40</sub>Cr<sub>40</sub>Ni<sub>20</sub> (at%) MPEA weighing 8 kg was prepared by vacuum induction melting. Fe, Cr, and Ni raw materials had purities  $\geq 99.9\%$  (wt %). Alloy smelting was carried out in an argon atmosphere to prevent oxidation. The molten metal was poured into a steel mold and then cooled to room temperature. The cast ingot was processed on a lathe to form a cylindrical ingot with a diameter of 120 mm and a height of 180 mm. The cylindrical ingot underwent solid solution treatment at 1200 °C for 24 h followed by water quenching to eliminate element segregation and intermetallic compound. Scanning electron microscopy (SEM, ZEISS-sigma), energy-dispersive X-ray spectrometry (EDS), electron backscatter diffraction (EBSD), and transmission electron microscopy (TEM, FEI Tecnai F30) were employed to characterize the microstructure. The size of the SEM and EBSD samples for the solid solution alloy was 10 mm × 10 mm × 8 mm. The samples were mechanically polished to 3000-grit SiC paper. To eliminate scratches, the specimens underwent electro-polishing in a solution of 90 vol% ethanol (C<sub>2</sub>H<sub>5</sub>OH) and 10 vol % perchloric acid (HClO<sub>4</sub>) using a 30 V voltage for 20–30 s. After cleaning in an alcohol solution, etching was performed using a mixed solution of 75 mL HCl and 25 mL HNO<sub>3</sub> for 10–20 s. The step size for the EBSD scan was 2.5  $\mu\text{m}$ . Iron FCC and BCC phases were selected for EBSD scans. EBSD tests were conducted for three times to calculate the average phase volume fraction. The flat dog bone-shaped tensile specimens with a gauge length of 8 mm, width of 4 mm, and thickness of 1.5 mm were prepared. Tensile tests were performed at 77 K for three times with a strain rate of  $1 \times 10^{-3}/\text{s}$ . The strain was measured using a contact extensometer. The temperature was controlled by liquid nitrogen. The tensile tests were interrupted at the strains of ~5 % and ~15 % to prepare the deformed samples. The unfractured tensile samples were cut equally into two parts, with one half used for EBSD testing and the other for TEM observation. The electro-polishing parameters of the deformed EBSD samples were the same as those of the solid solution treated samples. The step size for the deformed EBSD samples was 0.65  $\mu\text{m}$ . TEM samples with the size of  $\Phi 3 \text{ mm} \times 50 \mu\text{m}$  were fabricated via ion milling.

## 3. Results and discussion

**Fig. 1 (a)** and (b) show the SEM image and XRD pattern of the MPEA in the solid solution state, indicating that the alloy had an FCC + BCC dual-phase structure. The volume fractions of FCC and BCC phases were 49 % and 51 %, respectively. Another characteristic region containing grain boundary was selected for EBSD characterization to provide a clearer demonstration of the microstructure. The phase map and the inverse pole figure (IPF) map are shown in **Fig. 1(c)** and (d). The alloy was composed of FCC and BCC phases. BCC grains were clearly distinguished through crystallographic orientation, showing that the grain size of the BCC phase was large (>100  $\mu\text{m}$ ) after solid solution treatment. The FCC phase was fully surrounded by the BCC phase. At BCC grain boundary, the FCC phase was large in size and continuously distributed along the grain boundary. However, inside BCC grains, the irregularly shaped FCC phase was relatively small and dispersedly distributed in the BCC matrix. **Fig. 1(e)** shows the SEM-EDS elemental distribution maps. The difference between Cr and Ni in the two phases was very distinct. Cr was concentrated in the BCC phase, while the FCC phase had a higher Ni content. Fe was relatively high in the FCC phase. The chemical compositions of FCC and BCC phases are listed in **Table 1**.

**Fig. 2(a)** shows the tensile stress-strain curves of the Fe<sub>40</sub>Cr<sub>40</sub>Ni<sub>20</sub> MPEA at 298K and 77 K. The strength and ductility at 77K were significantly superior to those at 298K. At 77K, the Fe<sub>40</sub>Cr<sub>40</sub>Ni<sub>20</sub> MPEA exhibited a yield strength of 658 MPa (495 MPa at 298K), engineering ultimate tensile strength of 1388 MPa (827 MPa at 298K), and engineering elongation of 34.4 % (17 % at 298K). The true ultimate strength reached 1870 MPa, and the true elongation was 29.4 %. The cryogenic strength of the Fe<sub>40</sub>Cr<sub>40</sub>Ni<sub>20</sub> MPEA was higher than some reported FCC MPEAs, but the elongation was lower than theirs [7,8,11,13–18,21–23]. Compared to FCC-based dual-phase MPEAs (FCC + BCC/B2), the yield strength of the Fe<sub>40</sub>Cr<sub>40</sub>Ni<sub>20</sub> MPEA was slightly lower, while the ductility was not significantly different [11,19,20]. The strain hardening rate curves at 298K and 77 K are shown in **Fig. 2(b)**. The strain hardening ability at 77K was stronger than that at 298K. It indicates that the alloy exhibited strong strain hardening ability, especially in the early and middle stages (true strain <20 %). When the true strain was less than 20 %, the strain hardening rate was significantly higher than some reported MPEAs (see Supplementary Material). Considering the importance of density and cost in cryogenic applications, the comparison of the raw materials cost and the specific yield strength for Fe<sub>40</sub>Cr<sub>40</sub>Ni<sub>20</sub> MPEA with other reported MPEAs is shown in **Fig. 3(c)**. The calculation method of specific yield strength is shown in Supplementary Material. The present Fe<sub>40</sub>Cr<sub>40</sub>Ni<sub>20</sub> MPEA demonstrated a combination of specific yield strength  $\sim 84.36 \text{ MPa cm}^3/\text{g}$  and raw materials cost  $\sim 8343 \text{ USD/ton}$ , which was better than some reported MPEAs. Notably, the Fe<sub>40</sub>Cr<sub>40</sub>Ni<sub>20</sub> MPEA demonstrated exceptional properties through a simplified process of casting and solution treatment, leading to significant cost savings compared to other complex alloy production methods. It makes the Fe<sub>40</sub>Cr<sub>40</sub>Ni<sub>20</sub> MPEA a promising engineering material for cryogenic applications.

The microstructures deformed at different strains were observed to elucidate the cryogenic strengthening and deformation mechanisms. **Fig. 3** shows the deformation structure at a strain of ~5 %. The EBSD results are indicated in **Fig. 3(a)–(c)**. **Fig. 3(a)** and (b) demonstrate the presence of deformation twins in the BCC phase, while twinning did not occur in the FCC phase at this stage. The kernel average misorientation (KAM) map in **Fig. 3(c)** indicates that the dislocation density in the FCC phase was significantly higher than in the BCC phase. Simultaneously, the dislocation density at the phase boundaries was higher than that inside the FCC phase, suggesting that dislocations tended to accumulate at the phase boundary, as white arrows pointed. In addition, new orientations were found in the FCC phase, as indicated by the red arrows in **Fig. 3(b)** and (c). The formation of the new orientations primarily stemmed from crystal rotation. Gao et al. [23] found that dislocation pileups facilitated the crystal rotation. In this MPEA, the locations of

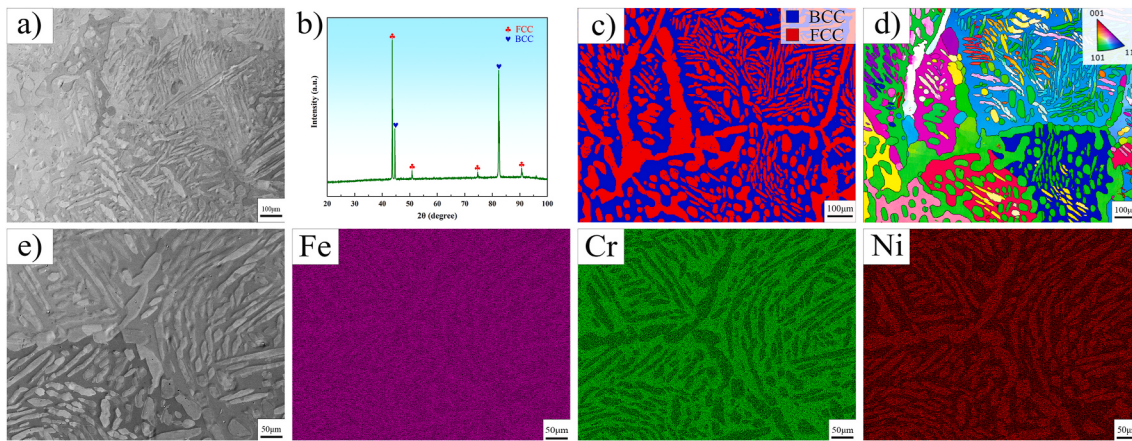


**Fig. 1.** (a) The SEM image of the MPEA; (b) the XRD pattern of the MPEA; (c) the EBSD phase map; (d) the EBSD IPF map; (e) SEM-EDS elemental distribution maps.

**Table 1**  
Chemical compositions of two phases (at%).

Phase	Fe	Cr	Ni
FCC	41.66	33.70	24.65
BCC	38.69	45.70	15.61

crystal rotation were often accompanied by severe dislocation pileup, as shown in Fig. 3(c). This indicates that these regions experienced higher stress, creating favorable conditions for crystal rotation. Fig. 3(d) shows the bright-field (BF) image of the phase boundary. A large number of dislocations were observed in the FCC phase, while dislocations were rarely observed in the BCC phase. Fig. 3(e) and (f) indicate the dislocation configuration in the FCC phase and the corresponding selected

area electron diffraction (SAED). Dislocations on multiple {111} slip planes were activated, resulting in dislocation tangles. Fig. 3(g) shows the twin boundary in the BCC phase. The SAEDs of the matrix and twin are shown in Fig. 3(g1) and (g2). The lamella phase formed between the matrix and the twin can be clearly observed. Fig. 3(g3) shows the SAED pattern of the blue region in Fig. 3(g), which includes the BCC matrix, deformation twin, and the lamella phase. The deformation twin was the common {112} twins in the BCC phase. The lamella phase was identified as the  $\omega$  phase with a hexagonal structure. The orientation relationship between the BCC matrix and the  $\omega$  phase was as follows: [011]<sub>BCC</sub>//[-1-120] <sub>$\omega$</sub> , (-21-1)<sub>BCC</sub>//(1-100) <sub>$\omega$</sub> . Fig. 3(g4) shows the dark-field (DF) image of  $\omega$  phase. Fig. 3(h) shows the high-resolution TEM (HR-TEM) image of the  $\omega$  phase.

Fig. 4 shows the deformation structure at a strain of ~15 %. The

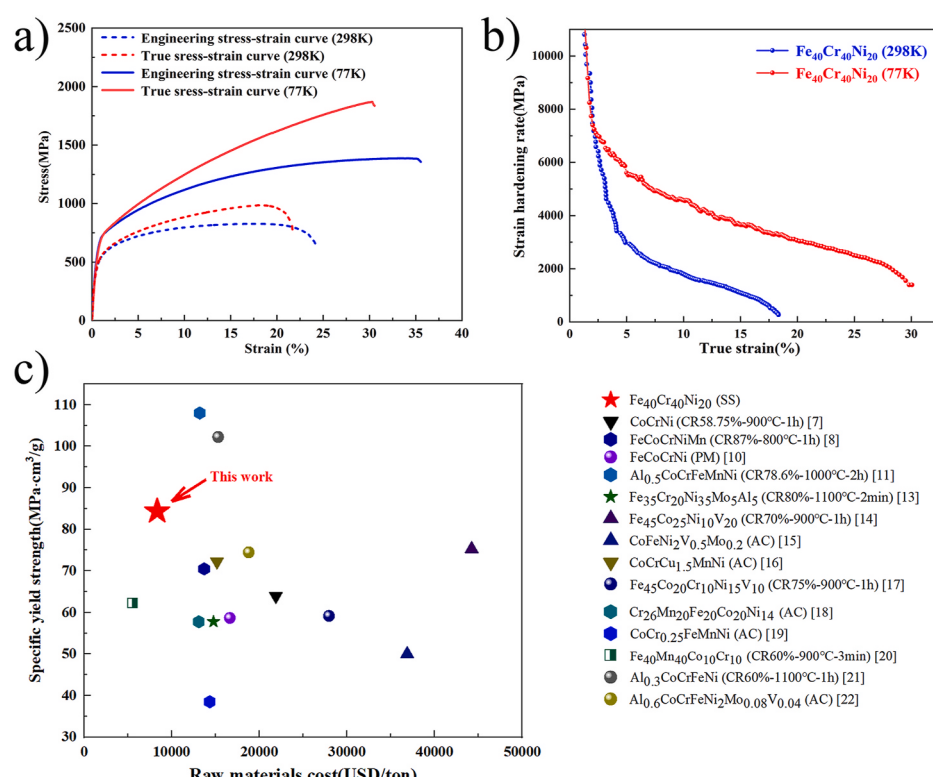


**Fig. 2.** (a) Tensile stress-strain curves of the Fe<sub>40</sub>Cr<sub>40</sub>Ni<sub>20</sub> MPEA at 298K and 77 K; (b) the strain hardening rate curves at 289K and 77 K; (c) Comparison of the cost of raw materials and the specific yield strength (77K) for Fe<sub>40</sub>Cr<sub>40</sub>Ni<sub>20</sub> MPEA with other reported MPEAs. (Annotation: SS-Solid solution; CR-Cold rolling; AC-As cast; PM-Power metallurgy).

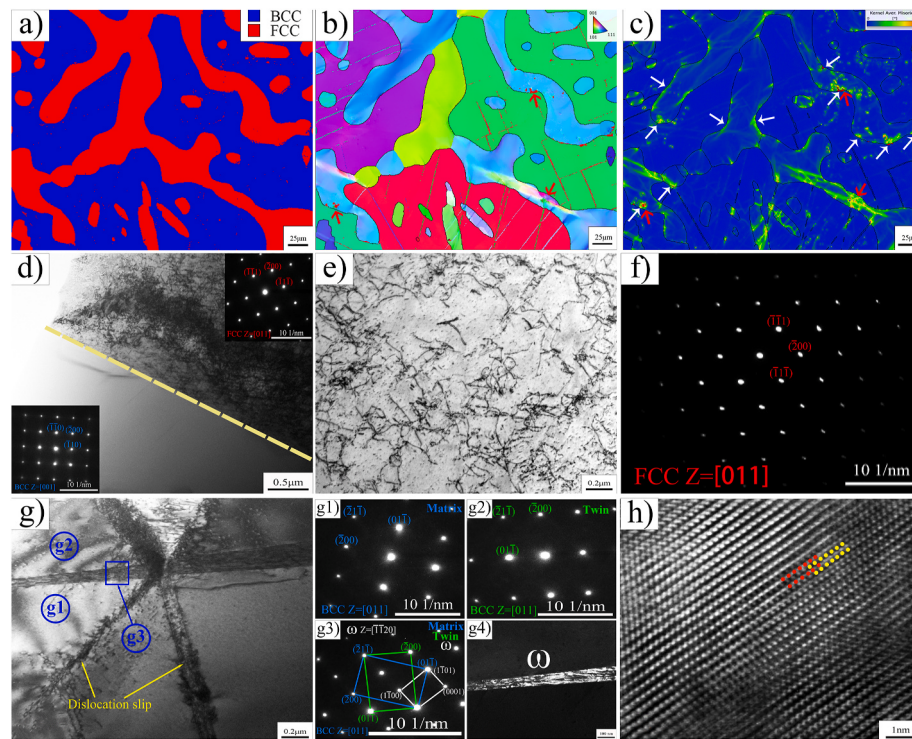


**Fig. 3.** The deformation structure at a strain of  $\sim 5\%$ . (a) The EBSD phase map; (b) the IPF map; (c) the KAM map; (d) the BF image of FCC and BCC phases and the corresponding SAED patterns; (e) dislocations in the deformed FCC phase; (f) the SAED of the FCC phase in (e); (g) the deformed BCC phase; (g1) - (g3) the SAED patterns of g1, g2, and g3 regions in (g); (g4) the DF image of the  $\omega$  phase; (h) the HR-TEM image of the  $\omega$  phase.

EBSD results are shown in Fig. 4(a)–(c). The dislocation density in the FCC phase and the number of deformation twins in the BCC phase were significantly increased compared to the early stage (strain  $\sim 5\%$ ). Fig. 4

(d) shows the phase boundary of two phases. When the strain reached  $15\%$ , a high density of deformation twins was also observed in the FCC phase, as confirmed by the SAED in Fig. 4(e). The DF image of FCC

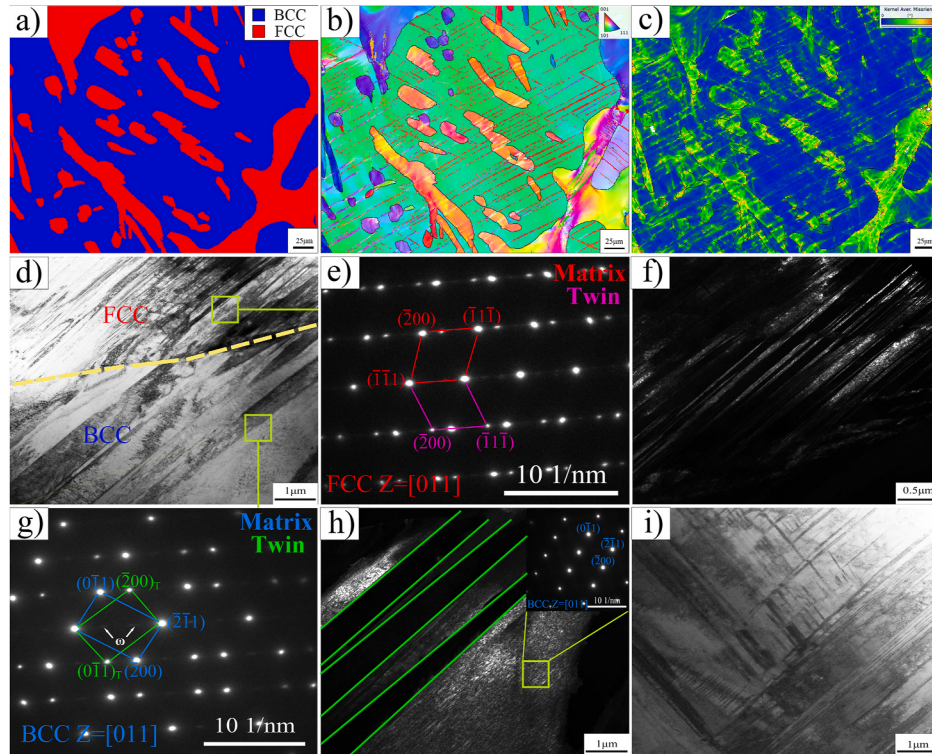


**Fig. 4.** The deformation structure at a strain of  $\sim 15\%$ . (a) The EBSD phase map; (b) the IPF map; (c) the KAM map; (d) the BF image of FCC and BCC phases; (e) the SAED pattern of the deformation twin; (f) the DF image of deformation twins in the FCC phase; (g) the SAED pattern of the deformation twin in the BCC phase; (h) the DF image of the deformed BCC matrix; (i) high density of deformation twins in the BCC phase.

deformation twins is shown in Fig. 4(f). It is worth emphasizing that the high-density deformation twins in the FCC phase were not reflected in the IPF map (Fig. 4(b)). This is primarily attributable to the small width of the deformation twins, less than 200 nm, while the step size of EBSD scan is 650 nm. The SAED in Fig. 4(g) confirms the formation of {112} deformation twins in the BCC phase. Meanwhile, the weak spots pointed by white arrows confirm the formation of the  $\omega$  phase. The DF image of the BCC matrix is displayed in Fig. 4(h). Twin boundaries were marked by the green line. A high density of dislocations was found in the BCC matrix near the twin boundaries. Fig. 4(i) indicates the {112} deformation twins with two different directions.

Based on the aforementioned deformed microstructures, the following three issues were discussed in detail:

- (1) The  $\omega$  phase. The  $\omega$  phase was a metastable phase commonly found in Ti alloys [24,25]. The  $\omega$  phase has also been sporadically observed in other BCC alloys, such as carbon steel [26,27] and Fe-Mn-Al alloy [28]. In this work, the  $\omega$  phase formed at the twin boundary within the BCC phase, thus called interfacial-twin-boundary- $\omega$  (ITB- $\omega$ ) [29]. The formation of ITB- $\omega$  was closely related to the {112}<111> deformation twins in the BCC phase, which was stress-induced. The formation of stress-induced  $\omega$  phase was mainly attributed to the glide of 1/3<111>, 1/6<111>, and 1/12<111> partial dislocations on different {112} planes [30]. The  $\omega$  phase, BCC matrix, and {112}<111> deformation twin maintained an orientation relationship: {1100} $_{\omega}$ //{112}<sub>BCC</sub>//{112}<sub>twin</sub>, as shown in Fig. 3(g3). According to the HR-TEM image in Fig. 3(h), two  $\omega$ -lattices (red and yellow) could be observed within the  $\omega$  phase. This indicates that the ITB- $\omega$  was formed by merging multiple  $\omega$  phases with the same crystal lattice structure. Similar phenomena have also been observed in Ti-9Cr-0.2O and Ti-10Cr alloys [31]. Many studies have shown that the formation of ITB- $\omega$  is often accompanied by stress relief [29,32], indicating that the formation of ITB- $\omega$  can release local stress concentration. When the strain was 5 %, no dislocation pile-up at the twin boundary was observed in the KAM map (Fig. 3(c)). However, dislocation pile-ups at the twin boundary in the BCC phase could be observed in the TEM image, as displayed in Fig. 3(g). This may be related to the low dislocation density. When the strain increased to 15 %, the dislocation density near the twin boundary in BCC phases significantly increased (Fig. 4(c) and (h)), indicating considerable stress concentration at the twin boundary. Therefore, in the BCC phase, ITB- $\omega$  was activated to release stress concentration caused by dislocation pile-up at the twin boundary.
- (2) Deformation mechanism. At a strain level of 5 %, deformation in the FCC phase predominantly relied on dislocation slip. At this stage, multiple slip systems were activated. Due to the relatively low stress, the dislocation density within the FCC phase was not high, as illustrated in Fig. 3(c). When the strain increased to 15 %, the dislocation density inside the FCC phase dramatically increased, as shown in Fig. 4(c). Simultaneously, a high density of nano deformation twins was formed to assist in deformation. The widths of these deformation twins ranged from approximately 10 to 200 nm. The deformation mechanism of the FCC phase transitioned from dislocation slip to twinning as the strain increased. This transition in deformation mechanism was very similar to some FCC MPEAs, such as CoCrNi [7], FeCoCrNiMn [8]. Furthermore, for some MPEAs with lower stacking fault energy, stress-induced martensitic transformation replaced twinning as the main deformation mechanism. For example, the Fe<sub>45</sub>Co<sub>25</sub>Ni<sub>10</sub>V<sub>20</sub> MPEA displayed an ultrahigh fracture elongation of 82 % with the aid of the martensitic transformation [14]. Although the deformation mechanism of the FCC phase was similar to other FCC MPEAs, the high BCC volume fraction resulted in inferior ductility for the Fe<sub>40</sub>Cr<sub>40</sub>Ni<sub>20</sub> MPEA compared to other FCC

MPEAs. The deformation ability of the BCC phase was inferior to that of the FCC phase, especially at cryogenic temperatures where it is prone to becoming brittle [33–35]. However, the BCC phase in the Fe<sub>40</sub>Cr<sub>40</sub>Ni<sub>20</sub> MPEA showed excellent deformation ability. In the early stage, twinning occurred in the BCC phase, and the number of deformation twins increased sharply with the increase in strain. Although dislocation slip existed in the BCC matrix, the dislocation density was not high. This suggests that deformation in the BCC phase predominantly depended on twinning. Furthermore, the formation of ITB- $\omega$  in the BCC phase released stress concentration at twin boundaries, effectively preventing microcrack formation. The contribution of ITB- $\omega$  to the ductility can not be overlooked. Thus, twinning in the two phases was the primary reason for the excellent cryogenic ductility.

- (3) Strengthening mechanism. In this work, the Fe<sub>40</sub>Cr<sub>40</sub>Ni<sub>20</sub> MPEA showed high strength and strong strain hardening ability at 77 K. The microstructural characterization showed that the alloy comprised only disordered FCC and BCC solid solutions with coarse grains. In addition to the solid solution strengthening contribution, its high strength was mainly related to its microstructural morphology and deformation mechanisms. Firstly, the alloy exhibited a typical dual-phase heterostructure, in which the BCC phase served as the hard phase while the FCC phase served as the soft phase. In this heterostructure, the FCC phase typically initiated plastic deformation before the BCC phase due to the low deformation resistance. Geometrically necessary dislocations (GNDs) accumulated at hetero-boundary within the FCC phase, creating back stress that impeded the motion of subsequent dislocations, thereby strengthening the FCC phase [36]. When the strain was 5 %, dislocations started moving first in the FCC phase. At this point, the density of GNDs inside the FCC phase was significantly lower than the hetero-boundary (as shown in Fig. 3(c)), leading to the generation of back stress that effectively enhanced the strength of the FCC phase. When the strain reached 15 %, the GND density in the FCC phase significantly increased. At this stage, besides the back stresses, dislocation strengthening also played a crucial role in enhancing the strength of the FCC phase. It is worth mentioning that the heterostructure in this alloy is different from most heterostructures reported previously, such as lamellar heterostructures [37,38] or heterostructures with a high volume fraction of soft zones [39,40]. The soft zone is continuous in the most reported heterostructures, whereas the hard zone is discontinuous. This implies that the soft zones can deform freely in certain directions. The deformation of the soft zones is not completely constrained; here, we refer to this as a partially constrained heterostructure. However, in the Fe<sub>40</sub>Cr<sub>40</sub>Ni<sub>20</sub> MPEA, the soft FCC phase was completely enveloped by the hard BCC phase, thus termed as a fully constrained heterostructure. In this fully constrained heterostructure, the deformation of the soft FCC phase was constrained in all directions, leading to a stronger back stress strengthening effect. Furthermore, the strong back stress made subsequent dislocation movement more challenging, resulting in a higher dislocation accumulation rate than the partially constrained heterostructure. A. Chauhan et al. [41–43] studied the back stress evolution of CoCrFeMnNi and CrFeNi MPEAs under low-cycle fatigue condition, revealing that the back stress was closely related to dislocation structures. The increase in dislocation density can effectively enhance the back stress strengthening [42]. Therefore, the rapid dislocation multiplication caused by fully constrain was an important reason for the enhancement of back stress strengthening. Zhu et al. [44] proposed that an ideal heterostructure should be designed to have the soft zones embedded in hard zones with certain deformability, thus maximizing the back stress strengthening effect. To the best of our knowledge, this kind of heterostructure has only been achieved in pure Ti through

rolling to form heterostructures composed of coarse and fine grains [45]. Our study shows that this fully constrained heterostructure can also be achieved by adjusting the volume fraction of two phases through composition design and heat treatment. Secondly, the "dynamic Hall-Petch effect" generated by deformation twinning was another important factor contributing to the high strength. Twin boundary strongly hindered dislocation movement, which could significantly enhance the strain hardening ability of the alloy [7]. In the Fe<sub>40</sub>Cr<sub>40</sub>Ni<sub>20</sub> MPEA, twinning was the primary deformation mechanism of the BCC phase. When the strain reached 5 %, multiple {112} twins were activated. These deformation twins intersected with each other, partitioning the matrix into several small regions, thereby achieving "dynamic grain refinement," as shown in Fig. 3(b). As strain increased, more {112} deformation twins became activated, leading to a decrease in the size of the divided regions. The distance between parallel twins was refined to tens to hundreds of nanometers, as depicted in Fig. 4(i). Similarly, the distance of nano deformation twins in the FCC phase was also below 200 nm, as shown in Fig. 4(f). The "dynamic grain refinement" induced by deformation twinning reduced the dislocation mean free path to tens to hundreds of nanometers. The strain hardening rate showed a negative correlation with the dislocation mean free path [46]. Consequently, the high strength of the Fe<sub>40</sub>Cr<sub>40</sub>Ni<sub>20</sub> MPEA was closely linked to deformation twinning.

- (4) Fracture mechanism. Fig. 5 shows the microstructure after fracture at 77 K. The microstructure morphology on the longitudinal section near the fracture is shown in Fig. 5(a). Cracks formed at the phase boundary rather than within the two phases, as indicated in Fig. 5(b). Fig. 5(c) shows the microstructure further away from the fracture. In this region, the stress was lower than that near the fracture. No cracks were found, indicating that cracks initially formed at phase boundaries as the stress increased. Fig. 5(d) shows the fracture morphology. Two different regions were marked by red and blue boxes. Fig. 5(e) indicates that dimples formed in the red region. The blue region exhibited fan-shaped and ligule patterns, as shown in Fig. 5(f). It indicates that the fracture mode is quasi-cleavage fracture. Based on the above observations, the fracture process of the Fe<sub>40</sub>Cr<sub>40</sub>Ni<sub>20</sub> MPEA at 77 K is as follows: During deformation, dislocations in the FCC phase proliferated and accumulated at phase boundaries, as indicated in Figs. 3(c) and 4(c). The stress concentration resulting from dislocation accumulation impacted both the phase boundary and the BCC phase. The BCC phase could release this stress

through twinning, thus, cracks first initiated at phase boundaries (Fig. 5(b)). As stress increased, the cracks propagated along the cleavage plane in the BCC matrix, the fan-shaped patterns in Fig. 5(f) confirms this point. During propagation, cleavage cracks encountered {112} deformation twins, and the interaction between them resulted in the formation of numerous ligule patterns. Finally, the connection of cleavage cracks led to fracture. It is worth noting that the deformation twins in the BCC matrix can be seen as obstacles to cleavage cracks, which can enhance the toughness at cryogenic temperatures.

#### 4. Conclusions

This work reported the cryogenic mechanical properties and underlying strengthening/deformation mechanisms of a cost-effective Fe<sub>40</sub>Cr<sub>40</sub>Ni<sub>20</sub> MPEA. The major conclusions are summarized as follows:

- (1) The MPEA had the FCC/BCC dual-phase structure in a solid solution state. The alloy exhibited excellent mechanical properties at 77 K with a yield strength of ~658 MPa, engineering/true ultimate tensile strength of ~1388/1870 MPa, and engineering/true elongation of ~34.4 %/29.4 %. The alloy demonstrated a good match between the specific yield strength and the cost of raw materials.
- (2) Deformation mechanism. At the early stage of plastic deformation, deformation in the FCC phase primarily depended on dislocation slip. As strain increased, the deformation mechanism shifted from dislocation slip to twinning. Deformation in the BCC phase relied on {112} plane twinning. The formation of ITB- $\omega$  could release the stress concentration at the {112} twin boundaries, which could improve the ductility of the BCC phase.
- (3) Strengthening mechanism. On the one hand, a fully constrained heterogeneous structure was obtained, with the soft FCC phase completely enveloped by the hard BCC phase. As the deformation of the soft FCC phase was fully constrained, the back stress strengthening effect became stronger. At the same time, the dislocation density inside the FCC phase increased rapidly, resulting in a stronger back strength strengthening effect. On the other hand, the formation of a high density of deformation twins in both phases could reduce the dislocation mean free path, thereby strengthening the alloy.

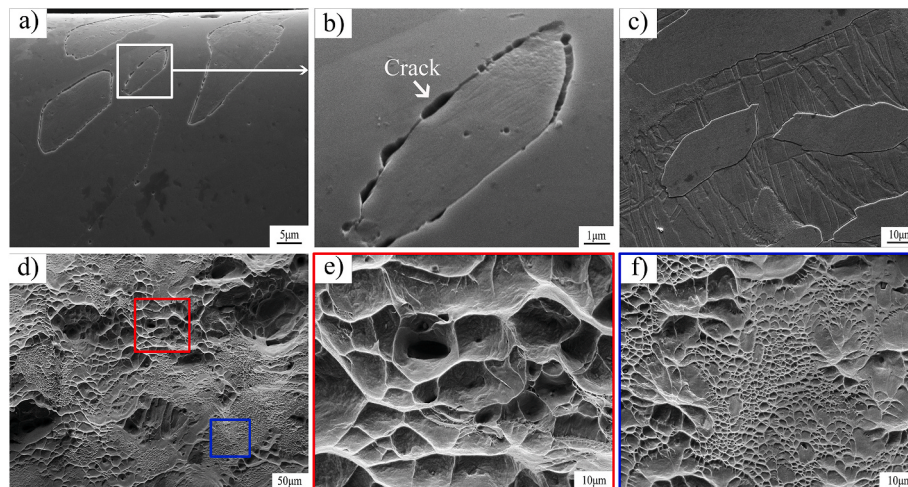


**Fig. 5.** The microstructure of the fractured sample. (a) The morphology of the FCC + BCC dual-phase structure near the fracture; (b) the crack at phase boundary; (c) the microstructure away from the fracture; (d) the fracture of the tensile sample; (e) dimples; (f) fan-shaped and ligule patterns.

## Data availability

The raw/processed data required to reproduce these findings cannot be shared at this time as the data also forms part of an ongoing study.

## Originality statement

I write on behalf of myself and all co-authors to confirm that the results reported in the manuscript are original and neither the entire work, nor any of its parts have been previously published. The authors confirm that the article has not been submitted to peer review, nor has been accepted for publishing in another journal. The authors confirms that the research in their work is original, and that all the data given in the article are real and authentic. If necessary, the article can be recalculated, and errors corrected.

## CRediT authorship contribution statement

**Jinrong Wang:** Writing – review & editing, Writing – original draft, Investigation. **Anguo Wang:** Methodology, Investigation. **Lu Zhang:** Writing – review & editing, Methodology, Investigation, Conceptualization. **Junyang Wang:** Investigation. **Li Zhang:** Investigation. **Rui Zhang:** Investigation. **Minghui Cai:** Investigation. **Jianxin Yu:** Investigation. **Baolin Wu:** Conceptualization.

## Declaration of competing interest

The authors declare that they have no known competing financial interests or personal relationships that could have appeared to influence the work reported in this paper.

## Acknowledgments

This work was financially supported by Basic scientific project of Liaoning Provincial Department of Education (JYTM20230264 and LJKMZ20220542), the fundamental research funds for the universities of Liaoning province and National College Student Innovation and Entrepreneurship Training Program Project (D202311052321377712) in Shenyang Aerospace University. The authors would like to thank the electron microscope center of KAIPLE Co. Ltd (Changsha) for the support of microstructural characterizations.

## Appendix A. Supplementary data

Supplementary data to this article can be found online at <https://doi.org/10.1016/j.msea.2024.147365>.

## Data availability

The authors are unable or have chosen not to specify which data has been used.

## References

- [1] B. Wang, Y. Huang, J. Wu, T. Wang, G. Lei, Experimental study on pressure control of liquid nitrogen tank by thermodynamic vent system, *Appl. Therm. Eng.* 125 (2017) 1037–1046.
- [2] D.W. Seo, D.H. Jung, J.T. Kwon, B.C. Choi, Numerical investigation of subcooled two-phase flow and heat transfer characteristics in a liquefied natural gas cargo containment system, *J. Nat. Gas Sci. Eng.* 121 (2024) 205–179.
- [3] Y. Bagheri, H. Kamali, E. Kamali, S.H. Nedjad, Formation of nodular bainite in an Fe-9.10Ni-0.06C (wt. %) alloy: a new microstructure for cryogenic steels, *Scripta Mater.* 208 (2022) 114–343.
- [4] T. Xu, Y. Shi, Z. Jiang, L. Wu, Y. Ma, Z. Wang, Improvement of cryogenic toughness for 9% Ni steel keyhole TIG butt-welded joints with a Ni interlayer, *Mater. Sci. Eng.* 835 (2022) 142–661.
- [5] S. Hany, M. Milochova, K. Littrell, R. Lorange, J.B. Vogt, E. Abi-Aad, E. Bychkov, Advanced characterization of cryogenic 9Ni steel using synchrotron radiation, neutron scattering and 57Fe Mössbauer spectroscopy, *Mater. Des.* 146 (2018) 219–227.
- [6] Y. Zhang, T.T. Zuo, Z. Tang, M.C. Gao, K.A. Dahmen, P.K. Liaw, Z.P. Lu, Microstructures and properties of high-entropy alloys, *Prog. Mater. Sci.* 61 (2014) 1–93.
- [7] G. Laplanche, A. Kostka, C. Reinhart, J. Hunfeld, G. Eggeler, E.P. George, Reasons for the superior mechanical properties of medium-entropy CrCoNi compared to high-entropy CrMnFeCoNi, *Acta Mater.* 128 (2017) 292–303.
- [8] F. Otto, A. Dlouhý, C. Somsen, H. Bei, G. Eggeler, E.P. George, The influences of temperature and microstructure on the tensile properties of a CoCrFeMnNi high-entropy alloy, *Acta Mater.* 61 (2013) 5743–5755.
- [9] X. Gao, W. Jiang, Y. Lu, Z. Ding, J. Liu, W. Liu, G. Sha, T. Wang, T. Li, I.T.H. Chang, Y. Zhao, Excellent strength-ductility combination of Cr<sub>26</sub>Mn<sub>20</sub>Fe<sub>20</sub>Co<sub>20</sub>Ni<sub>14</sub> high-entropy alloy at cryogenic temperatures, *J. Mater. Sci. Technol.* 154 (2023) 166–177.
- [10] Y. Wang, Q. Liu, K. Yan, W. Wang, S. Kabra, Y.L. Chiu, D. Dye, P.D. Lee, Y. Liu, B. Cai, Probing deformation mechanisms of a FeCoCrNi high-entropy alloy at 293 and 77 K using in situ neutron diffraction, *Acta Mater.* 154 (2018) 79–89.
- [11] J.M. Park, J. Moon, J.W. Bae, D.H. Kim, Y.H. Jo, S. Lee, H.S. Kim, Role of BCC phase on tensile behavior of dual-phase Al<sub>0.5</sub>CoCrFeMnNi high-entropy alloy at cryogenic temperature, *Mater. Sci. Eng.* 746 (2019) 443–447.
- [12] C. Chu, W. Chen, L. Huang, H. Wang, L. Chen, Z. Fu, Exceptional strength-ductility synergy at room and liquid nitrogen temperatures of Al<sub>7.5</sub>Co<sub>20.5</sub>Fe<sub>24</sub>Ni<sub>24</sub>Cr<sub>24</sub> high-entropy alloy with hierarchical precipitate heterogeneous structure, *Int. J. Plast.* 175 (2024) 103939.
- [13] Y. Yin, W. Ren, Q. Tan, H. Chen, H. Huang, M.X. Zhang, A cost-effective cryogenic high-entropy alloy with high strength-ductility synergy and strain hardenability, *Mater. Sci. Eng.* 865 (2023) 144–607.
- [14] Y.X. Li, R.K. Nutor, Q.K. Zhao, X.P. Zhang, Q.P. Cao, S.S. Sohn, X.D. Wang, S. Q. Ding, D.X. Zhang, H.F. Zhou, J.W. Wang, J.Z. Jiang, Unraveling the deformation behavior of the Fe<sub>45</sub>Co<sub>25</sub>Ni<sub>10</sub>V<sub>20</sub> high entropy alloy, *Int. J. Plast.* 165 (2023) 103–619.
- [15] L. Jiang, Y.P. Lu, M. Song, C. Lu, K. Sun, Z.Q. Cao, T.M. Wang, F. Gao, L.M. Wang, A promising CoFeNi<sub>2</sub>V<sub>0.5</sub>Mo<sub>0.2</sub> high entropy alloy with exceptional ductility, *Scripta Mater.* 165 (2019) 128–133.
- [16] S.H. Shim, H. Pouraliakbar, B.J. Lee, Y.K. Kim, M.S. Rizi, S.I. Hong, Strengthening and deformation behavior of as-cast CoCrCu<sub>1.5</sub>MnNi high entropy alloy with micro-/nanoscale precipitation, *Mater. Sci. Eng.* 853 (2022) 143–729.
- [17] Y.H. Jo, K.Y. Doh, D.G. Kim, K. Lee, D.W. Kim, H. Sung, S.S. Sohn, D. Lee, H.S. Kim, B.J. Lee, S. Lee, Cryogenic-temperature fracture toughness analysis of non-equatomic V<sub>10</sub>Cr<sub>10</sub>Fe<sub>45</sub>Co<sub>20</sub>Ni<sub>15</sub> high-entropy alloy, *J. Alloys Compd.* 809 (2019) 151–864.
- [18] X. Gao, W. Jiang, Y. Lu, Z. Ding, J. Liu, W. Liu, G. Sha, T. Wang, T. Li, T.H. Chang, Y. Zhao, Excellent strength-ductility combination of Cr<sub>26</sub>Mn<sub>20</sub>Fe<sub>20</sub>Co<sub>20</sub>Ni<sub>14</sub> high-entropy alloy at cryogenic temperatures, *J. Mater. Sci. Technol.* 154 (2023) 166–177.
- [19] M.V. Klimova, A.O. Semenyuk, D.G. Shaysultanov, G.A. Salishchev, S. V. Zherebtsov, N.D. Stepanov, Effect of carbon on cryogenic tensile behavior of CoCrFeMnNi-type high entropy alloys, *J. Alloys Compd.* 811 (2019) 152000.
- [20] Z.F. He, N. Jia, D. Ma, H.L. Yan, Z.M. Li, D. Raabe, Joint contribution of transformation and twinning to the high strength-ductility combination of a FeMnCoCr high entropy alloy at cryogenic temperatures, *Mater. Sci. Eng.* 759 (2019) 437–447.
- [21] Q. Li, T.W. Zhang, J.W. Qiao, S.G. Ma, D. Zhao, P. Lu, B. Xu, Z.H. Wang, Superior tensile properties of Al<sub>0.3</sub>CoCrFeNi high entropy alloys with B2 precipitated phases at room and cryogenic temperatures, *Mater. Sci. Eng.* 767 (2019) 138–424.
- [22] Y. Dong, S. Duan, X. Huang, C. Li, Z. Zhang, Excellent strength-ductility synergy in as-cast Al<sub>0.6</sub>CoCrFeNi<sub>2</sub>Mo<sub>0.08</sub>V<sub>0.04</sub> high-entropy alloy at room and cryogenic temperatures, *Mater. Lett.* 294 (2021) 129–778.
- [23] F. Gao, Q. Zhu, W. Xue, Y. Chen, F. Zhang, Y. Nan, S. Tang, J. Zhang, D. Tie, X. Cai, F. Yu, Z. Liu, Correlation between formability, ridging and recrystallization texture development in ferritic stainless steel fabricated by introducing intermediate annealing during cold rolling, *Mater. Char.* 205 (2023) 113296.
- [24] M.J. Lai, T. Li, D. Raabe,  $\omega$  phase acts as a switch between dislocation channeling and joint twinning- and transformation-induced plasticity in a metastable  $\beta$  titanium alloy, *Acta Mater.* 151 (2018) 67–77.
- [25] W. Wang, X. Zhang, W. Mei, J. Sun, Role of omega phase evolution in plastic deformation of twinning-induced plasticity  $\beta$  Ti-12V-2Fe-1Al alloy, *Mater. Des.* 186 (2020) 108–282.
- [26] T. Liu, D. Zhang, Q. Liu, Y. Zheng, Y. Su, X. Zhao, J. Yin, M. Song, D. Ping, A new nanoscale metastable iron phase in carbon steels, *Sci. Rep.* 5 (2015) 15331.
- [27] D.H. Ping, W.T. Geng, A popular metastable omega phase in body-centered cubic steels, *Mater. Chem. Phys.* 139 (2013) 830–835.
- [28] H. Peng, X. Yang, L. Sun, L. Yong, J. Yan, J. Zhang, B. Qian, Y. Wen, Deformation-induced interfacial-twin-boundary  $\omega$ -phase in an Fe<sub>48</sub>Mn<sub>37</sub>Al<sub>15</sub> body-centered cubic metastable alloy, *J. Mater. Sci. Technol.* 146 (2023) 252–258.
- [29] S.Q. Wu, D.H. Ping, Y. Yamabe-Mitarai, W.L. Xiao, Y. Yang, Q.M. Hu, G.P. Li, R. Yang, {112}<111> Twinning during  $\omega$  to body-centered cubic transition, *Acta Mater.* 62 (2014) 122–128.
- [30] F. Sun, J.Y. Zhang, M. Marteleur, T. Gloriant, P. Vermaut, D. Laillé, P. Castany, C. Curfs, P.J. Jacques, F. Prima, Investigation of early stage deformation mechanisms in a metastable  $\beta$  titanium alloy showing combined twinning-induced plasticity and transformation-induced plasticity effects, *Acta Mater.* 61 (2013) 6406–6417.

- [31] H. Liu, M. Niinomi, M. Nakai, K. Cho, Athermal and deformation-induced  $\omega$ -phase transformations in biomedical beta-type alloy Ti-9Cr-0.20, *Acta Mater.* 106 (2016) 162–170.
- [32] Y. Yang, P. Castany, E. Bertrand, M. Cornen, J.X. Lin, T. Gloriant, Stress release-induced interfacial twin boundary  $\omega$  phase formation in a  $\beta$  type Ti-based single crystal displaying stress-induced  $\alpha''$  martensitic transformation, *Acta Mater.* 149 (2018) 97–107.
- [33] S.R. Ortner, The ductile-to-brittle transition in steels controlled by particle cracking, *Fatigue Fract. Eng. Mater. Struct.* 29 (2006) 752–769.
- [34] T. Sharma, N.N. Kumar, R. Mondal, K.V.M. Krishna, I. Samajdar, V. Kain, Ductile-to-Brittle transition in low-alloy steel: a combined experimental and numerical investigation, *J. Mater. Eng. Perform.* 28 (2019) 4275–4288.
- [35] T.D. Joseph, M. Tanaka, A.J. Wilkinson, S.G. Roberts, Brittle–ductile transitions in vanadium and iron–chromium, *J. Nucl. Mater.* 367–370 (2007) 637–643.
- [36] J. Niu, Z. Fu, W. Chen, T. Lu, L. Hao, W. Xiong, H. Wen, Hierarchical microstructure enables high strength and good ductility in as-cast Fe<sub>27</sub>Ni<sub>35</sub>Cr<sub>18.25</sub>Al<sub>13.75</sub>Co<sub>2</sub>Ti<sub>2</sub>Mo<sub>2</sub> high-entropy alloy, *J. Mater. Sci. Technol.* 179 (2024) 9–21.
- [37] J. Li, Y. Cao, B. Gao, Y. Li, Y. Zhu, Superior strength and ductility of 316L stainless steel with heterogeneous lamella structure, *J. Mater. Sci.* 53 (2018) 10442–10456.
- [38] Z.K. Li, X.T. Fang, Y.F. Wang, P. Jiang, J.J. Wang, C.M. Liu, X.L. Wu, Y.T. Zhu, C. Koch, Tuning heterostructures with powder metallurgy for high synergistic strengthening and hetero-deformation induced hardening, *Mater. Sci. Eng.* 777 (2020) 139074.
- [39] Y. Li, Y.H. Zhao, V. Ortalan, W. Liu, Z.H. Zhang, R.G. Vogt, N.D. Browning, E. J. Lavernia, J.M. Schoenung, Investigation of aluminum-based nanocomposites with ultra-high strength, *Mater. Sci. Eng.* 527 (2009) 305–316.
- [40] S.Y. Tung, T.E. Hsu, Y.T. Zhu, M.H. Tsai, Recrystallized hard zone and resultant trimodal microstructure produces superior mechanical properties in a single-phase heterostructured high-entropy alloy, *Acta Mater.* 273 (2024) 119957.
- [41] K. Lu, A. Chauhan, F. Knöpfle, J. Aktaa, Effective and back stresses evolution upon cycling a high-entropy alloy, *Mater. Res. Lett.* 10 (2022) 369–376.
- [42] S. Sisodia, M. Rajkowski, G. Laplanche, A. Chauhan, Cyclic deformation behavior of an equiatomic CrFeNi multi-principal element alloy, *Int. J. Fatig.* 174 (2023) 107723.
- [43] K. Lu, A. Chauhan, A.S. Tirunilai, J. Freudenberger, A. Kauffmann, M. Heilmair, J. Aktaa, Deformation mechanisms of CoCrFeMnNi high-entropy alloy under low-cycle-fatigue loading, *Acta Mater.* 215 (2021) 117089.
- [44] Y.T. Zhu, X.L. Wu, Heterostructured materials, *Prog. Mater. Sci.* 131 (2023) 101019.
- [45] X. Wu, M. Yang, F. Yuan, G. Wu, Y. Wei, X. Huang, Y. Zhu, Heterogeneous lamella structure unites ultrafine-grain strength with coarse-grain ductility, *Proc. Natl. Acad. Sci. U.S.A.* 112 (2015) 14501–14505.
- [46] U.F. Kocks, H. Mecking, Physics and phenomenology of strain hardening: the FCC case, *Prog. Mater. Sci.* 48 (2003) 171–273.